IEEE Access
Multidisciplinary | Rapid Review | Open Access Journal

Received January 11, 2019, accepted January 27, 2019, date of publication February 8, 2019, date of current version March 1, 2019.

Digital Object Identifier 10.1109/ACCESS.2019.2898262

Design and Experiments of a Novel Rotary Piezoelectric Actuator Using Longitudinal–Torsional Convertors

DEEN BAI, QIQUAN QUAN, (Member, IEEE), DEWEI TANG, AND ZONGQUAN DENG
State Key Laboratory of Robotics and System, Harbin Institute of Technology, Harbin 150001, China

Corresponding author: Qiquan Quan (quanqiquan@hit.edu.cn)

This work was supported in part by the National Natural Science Foundation of China under Grant 61403106, in part by the Program of Introducing Talents of Discipline to Universities under Grant B07018, and in part by the National Natural Science Foundation of China under Grant 51521003.

ABSTRACT A bolt-clamped type piezoelectric actuator, which could output rotary motions by using longitudinal–torsional hybrid vibration, was proposed and tested in this paper. The proposed actuator is mainly composed of a piezoelectric stack, a leftward bending longitudinal–torsional convertor (LBLTC), and a rightward bending longitudinal–torsional convertor (RBLTC). The piezoelectric stack, which is clamped between the LBLTC and RBLTC, is utilized to generate longitudinal vibration under exciting of a sinusoidal signal with a certain frequency. The two convertors transform part of the longitudinal vibration generated by the piezoelectric stack into the torsional vibration and generate elliptical motions at the ends of the driving tips, which can push the rotors to rotate step by step. The structure of the proposed actuator was designed, and the working principle for the rotary driving was analyzed. Then, modal, harmonic, and transient analyses were carried out by the finite element method to determine the structural dimensions of the convertors and verify the movement trajectories of the driving tips. Finally, a prototype was fabricated, and its vibration and output characteristics were tested. The experimental results indicated that the maximum no-load speed and maximum torque of the actuator were 342 r/min and 0.072 N·m under the preload of 11 N and the voltage of 300 V_{P_P}. The simulation and experimental results verified the feasibility of the proposed actuator.

INDEX TERMS Piezoelectric actuator, finite element method (FEM), ultrasonic motor, mode conversion type, longitudinal–torsional hybrid vibration, longitudinal-torsional convertor.

I. INTRODUCTION

The piezoelectric actuators usually use the inverse piezoelectric effect to convert the electrical energy into the vibration mechanical energy [1], and have long been investigated extensively and applied successfully in lots of fields [2]–[4]. Compared with the traditional electromagnetic motors, the piezoelectric actuators have the advantages of no electromagnetic radiation, self-locking, high power weight ratio, high displacement resolution [5]–[8], making it suitable for robots [9]–[11], high-precision machines [12]–[15], nanopositioning stages [16]–[18], optical instruments [16]–[18], bioengineer [19]–[21], and invasive surgery [12], [25], [26].

According to vibration characteristic, piezoelectric actuators can be classified into resonant type [27]–[29] and non-resonant type [30]–[32]. The non-resonant type piezoelectric actuators can realize precision motion control with a scale of nanometer, but they usually have short strokes or low speeds [33]. For example, Tang *et al.* [34] proposed a piezoelectric-actuator-driven nanopositioning stages which reached a workspace of 1.035×1.035 mm with a closed-loop positioning accuracy of 400 nm. The resonant type piezoelectric actuators have merits of simple structure, high torque, quick response, and self-lock when power off [33]. The resonant type piezoelectric actuators utilize the elliptical motions of the driving tips, which are generated by the converse piezoelectric effects of the piezoelectric elements, and friction coupling between the runner and the stator to push the runner. In general, the elliptical motions can be generated by two traveling waves with a certain phase difference [35]. Furthermore, the elliptical motions can also be formed by two standing waves, such as the hybrid of longitudinal and

The associate editor coordinating the review of this manuscript and approving it for publication was Yingxiang Liu.

bending vibrations [36]–[38], the hybrid of longitudinal and torsional vibrations [39], [40], and the hybrid of two bending vibrations [41].

The piezoelectric actuators, which use the hybrid of longitudinal and torsional vibrations, can be divided into multi-mode type [42], [43] and mode conversion type [44], [45]. The multi-mode type actuators use two groups of piezoelectric elements to generate the longitudinal vibration and torsional vibration, separately. When exciting voltages with a certain frequency are applied on the two groups, respectively, the longitudinal–torsional hybrid vibration will be generated. However, the proper longitudinal and torsional vibration modes must be used and the frequencies for the two modes must be same. By contrast, the mode conversion type actuators only have one group of piezoelectric elements for longitudinal vibration. A longitudinal-torsional convertor, which usually has special structural features, is utilized to transform part of the longitudinal vibration into the torsional vibration. Finally, the longitudinal–torsional hybrid vibration will be formed and the elliptical motions of the points on a driving surface can be generated.

Besides, the piezoelectric actuators can also be classified based on combine mode of the piezoelectric elements and metal blocks as bonded type [46] and bolt-clamped type [47], [48]. The piezoelectric elements of the bonded type actuators are glued on elastic metal blocks with conductive adhesive and adopt d_{31} working mode which exhibits a lower electromechanical coupling factor to excite the resonance vibrations. Fatigue of the adhesive layer caused by shear stress and fragility of the piezoelectric elements under strong extension stress limit their applications in harsh temperature environment [49]. The bolt-clamped type actuators, which usually clamp the piezoelectric elements between the metal blocks with a bolt, can apply larger preload on the piezoelectric elements. Hence, a higher exciting voltage can be applied to output larger power without the fatigue of the adhesive layer or the fragility of the piezoelectric elements. Moreover, the piezoelectric elements of the bolt-clamped type actuators work at d_{33} mode which has a higher energy transfer efficiency than the d_{31} mode.

This paper proposes and verifies a novel bolt-clamped type rotary piezoelectric actuator which makes use of two longitudinal-torsional convertors to generate elliptical motions. The proposed actuator not only inherits the merits of the bolt-clamped type actuators, but also can realize rotary driving. The remainder of this paper is organized as follows. In Section II, configuration and operating principle of the proposed actuator are presented. Detailed design process of the proposed actuator is discussed in Section III. The elliptical trajectories of the driving tips are verified by transient analysis in Section IV. In Section V, the vibration characteristic and output performance of the actuator are investigated with experiments. Finally, the conclusions are drawn in Section VI.

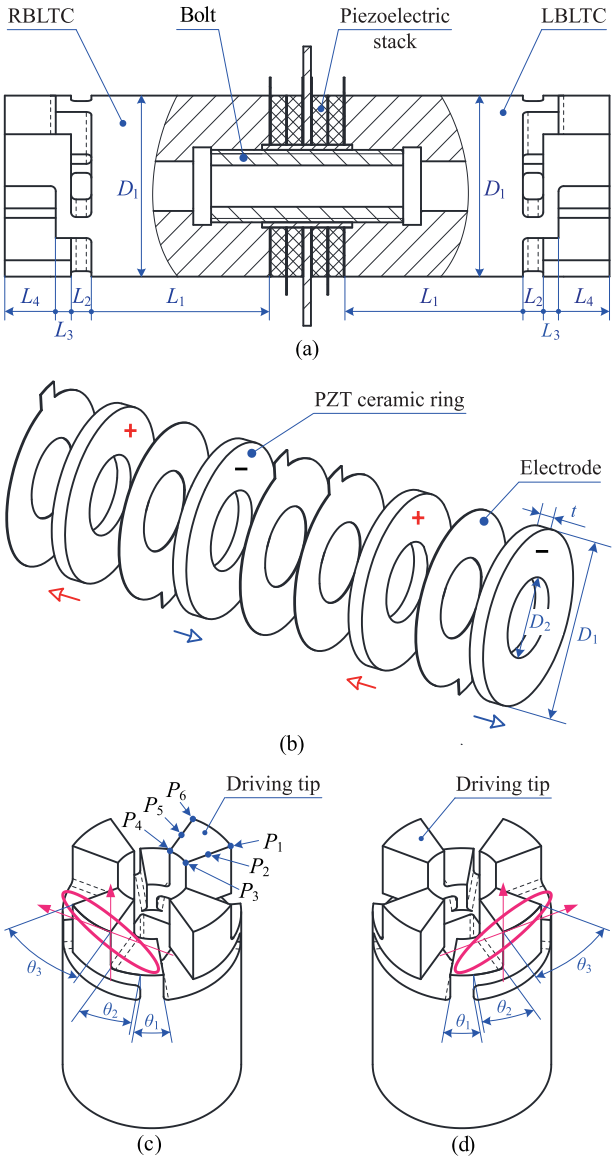

FIGURE 1. Configuration of the proposed actuator. (a) Broken-out section view. (b) Polarizations of the PZT ceramic rings. (c) Three-dimensional model of the LBLTC. (d) Three-dimensional model of the RBLTC.

II. CONFIGURATION AND OPERATING PRINCIPLE OF THE PROPOSED ACTUATOR

Configuration of the actuator is shown in Fig. 1. The actuator consists of a piezoelectric stack, a leftward bending longitudinal–torsional convertor(LBLTC), a rightward bending longitudinal–torsional convertor(RBLTC), and a bolt. The piezoelectric stack, which is compose of several electrodes and four lead zirconate titanate (PZT) ceramic rings, is clamped between the LBLTC and the RBLTC by the bolt, as shown in Fig. 1(a). The PZT ceramic rings are polarized along their thickness directions and the polarization directions of adjacent PZT ceramic rings are opposite, as shown in Fig. 1(b). Three-dimensional model of the LBLTC is shown in Fig. 1(c). The LBLTC, which includes four leftward bending driving tips on the top, converts part of the longitudinal vibration on one side of the piezoelectric stack into

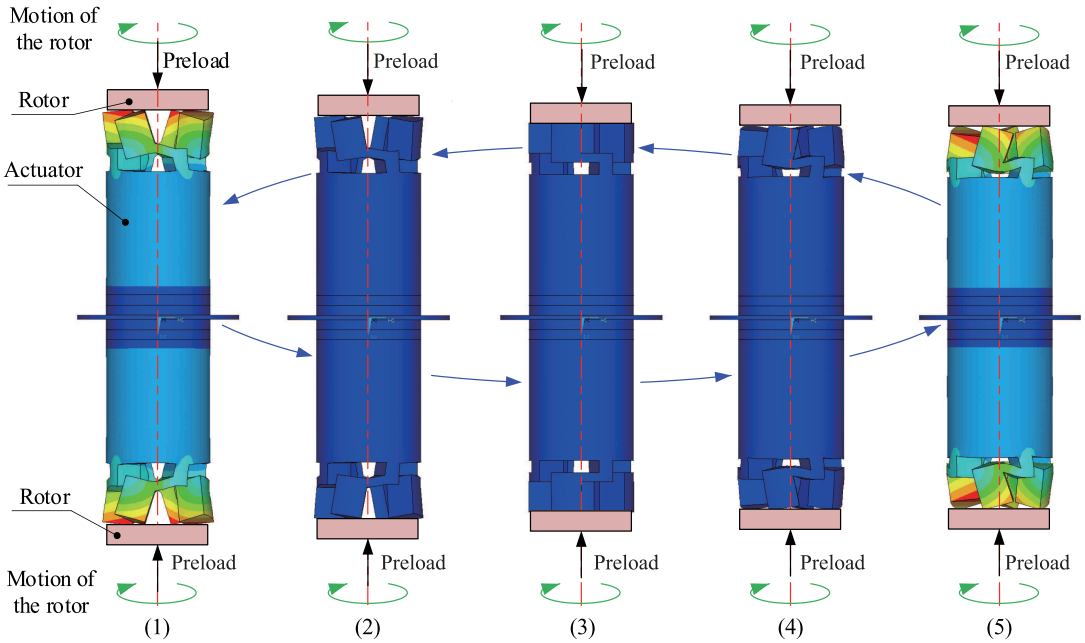

FIGURE 2. Working principle of the proposed actuator.

longitudinal-torsional vibration and forms leftward elliptical trajectories at the ends of the driving tips. The structural difference between the LBLTC and RBLTC is that the latter has four rightward bending driving tips, as shown in Fig. 1(d). Then the RBLTC utilizes the longitudinal vibration on the other side of the piezoelectric stack to generate rightward elliptical trajectories. Fig. 2 illustrates operating principle of the proposed actuator. Under the excitation of a sinusoidal voltage, the actuator vibration shape will change as (3)-(2)-(1)-(2)-(3)-(4)-(5)-(4)-(3). Then, elliptical trajectories are formed on the driving tips of the LBLTC and RBLTC simultaneously. Finally, the driving tips push two rotors to rotate around a certain axis using the frictional force provided by the vertical preload.

III. DESIGN OF THE PROPOSED ACTUATOR

The elliptical trajectories of the driving tips are affected by the structural dimensions of the actuator. The finite-element method (FEM, ANSYS software) was used to determine the effect of the structural dimensions on the vibration characteristic of the actuator. The materials of the LBLTC and RBLTC are both aluminum alloy with a mass density of 2700 kg/m^3, a Young's modulus of 7.17 $\times$ 10^{10} N/m^2 and a Poisson ratio of 0.32. The material of the bolt is stainless steel with a mass density of 7930 kg/m^3, a Young's modulus of 2.09 $\times$ 10^{11} N/m^2 and a Poisson ratio of 0.3. The material of the ceramic ring is PZT-8 (provided by Yu Hai Electronic ceramics Co., Ltd.). The mass density of the ceramic ring is 7600 kg/m^3, and its other physical parameters are as follows:

$$d = \begin{bmatrix} 0 & 0 & 0 & 0 & 33 & 0 \\ 0 & 0 & 0 & 33 & 0 & 0 \\ -9.7 & -9.7 & 22.5 & 0 & 0 & 0 \end{bmatrix} \times 10^{-11} \ \mathrm{C/N} \quad (1)$$

TABLE 1. Specific structure dimensions.

Simulation parameter	Values	Simulation parameter	Values
D_1	35 mm	L_3	3 mm
D_2	16 mm	L_4	10 mm
t	3 mm	θ_1	15°
L_1	40 mm	θ_2	20°
L_2	4 mm	θ_3	35°

$$\varepsilon^T = \begin{bmatrix} 11.4 & 0 & 0 \\ 0 & 11.4 & 0 \\ 0 & 0 & 8.9 \end{bmatrix} \times 10^{-9} \ \mathrm{F/m} \quad (2)$$

$$c^E = \begin{bmatrix} 14.7 & 8.1 & 8.1 & 0 & 0 & 0 \\ 8.1 & 14.7 & 8.1 & 0 & 0 & 0 \\ 8.1 & 8.1 & 13.2 & 0 & 0 & 0 \\ 0 & 0 & 0 & 3.3 & 0 & 0 \\ 0 & 0 & 0 & 0 & 3.1 & 0 \\ 0 & 0 & 0 & 0 & 0 & 3.1 \end{bmatrix} \times 10^{10} \ \mathrm{N/m^2} \quad (3)$$

where d, ε^T, and c^E are the piezoelectric matrix, the dielectric matrix, and the stiffness matrix, respectively.

During pushing the rotor, the two edges of each driving tip contact the rotor alternately, as shown in Fig. 2. Six points on two edges of one driving tip including P_1, P_2, P_3, P_4, P_5, and P_6 were selected, as shown in Fig. 1(c). The elliptical trajectory of each point was decomposed into axial vibration and circumferential vibration. The modal analysis and harmonic analysis were utilized to analyze the vibration amplitudes of the selected points in the axial and circumferential directions under different structural dimensions. Fig. 1(a)–(d) and Table 1 together show the initial structure dimensions

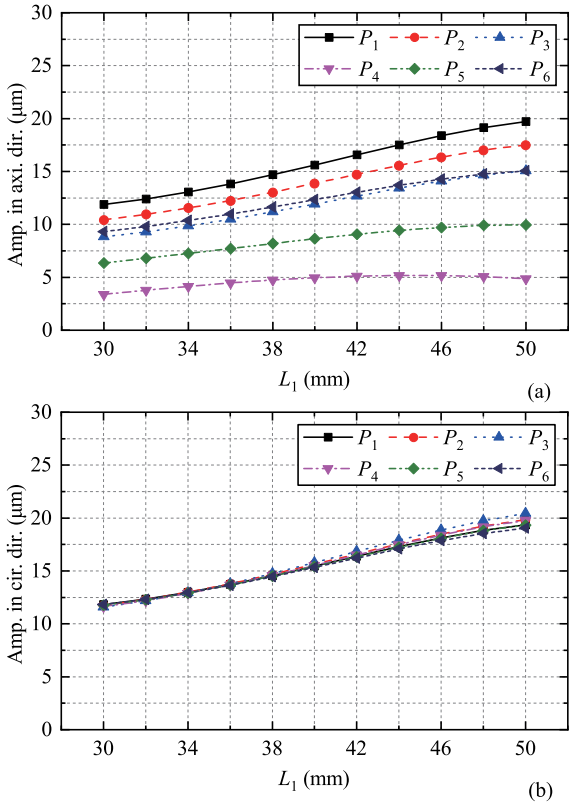

FIGURE 3. Displacement amplitudes of the selected points to different L_1. (a) Amplitudes in axial direction. (b) Amplitudes in circumferential direction.

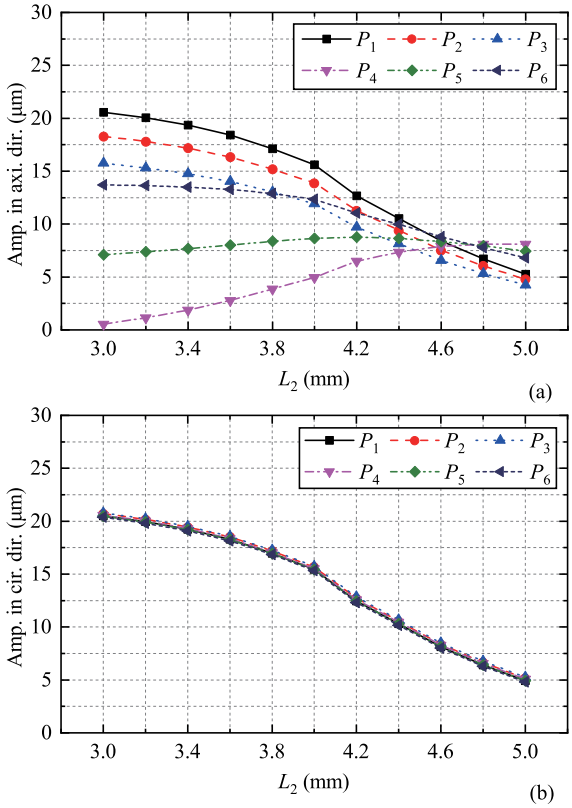

FIGURE 4. Displacement amplitudes of the selected points to different L_2. (a) Amplitudes in axial direction. (b) Amplitudes in circumferential direction.

of the actuator. Seven parameters including L_1, L_2, L_3, L_4, θ_1, θ_2, and θ_3 were selected and adjusted separately. During the simulations, the voltage amplitude and the damping ratio were set as 200 V and 0.0014, respectively.

The displacement amplitudes of the selected points in the axial and circumferential directions increase with the increase of L_1, as shown in Fig. 3. The amplitudes of the selected points in the axial direction are quite different. However, the circumferential displacement amplitudes of the selected points are less different. In addition, the points near the outer cylindrical surface of the actuator, P_1 and P_6, have larger axial displacement amplitudes than the points near the inner cylindrical surface of the actuator, such as P_3 and P_4.

It can be seen that increasing L_2 has a remarkable effect on the axial displacement amplitudes of the selected points, as shown in Fig. 4(a). The axial displacement amplitudes of P_1, P_2, P_3, and P_6 decrease with the increase of L_2, while that of P_4 increase with the increase of L_2. The amplitude of P_5 in the axial direction increases first and then decreases with the increase of L_2. Furthermore, the circumferential displacement amplitudes of the selected points decrease with the increase of L_2 and nearly have same values for each L_2, as shown in Fig. 4(b).

Fig. 5(a) indicates that with increasing L_3, the axial displacement amplitudes of P_1, P_2, P_3, and P_6 decrease slowly. However, the displacement amplitudes of P_4 and P_5 in the axial direction increase with the increase of L_3. Moreover, the circumferential displacement amplitudes of the selected points decrease with the increase of L_3, as shown in Fig. 5(b).

Fig. 6(a) shows that as L_4 increases from 5 mm to 15 mm, the axial displacement amplitudes of P_1, P_2, P_3, and P_6 and the circumferential displacement amplitudes of all the selected points increase first and then decrease, and reach their maximum values when the L_4 is about 12 mm. With increasing L_4, the axial displacement amplitude of P_5 increases in the initial phase and reaches its maximum value when L_4 is about 9 mm. Then, it decreases slowly. Furthermore, in the range of 5 mm to 15 mm, the axial displacement amplitude of P_4 decreases with the increase of L_4.

With increasing θ_1 in the range of 5° to 25°, the displacement amplitudes of P_1, P_2, P_3, and P_6 in the axial direction and of all the selected points in the circumferential direction increase gradually, as shown in Fig. 7(a) and (b). The axial displacement amplitudes of P_4 and P_5 reach their maximum values when θ_1 is equal to 11° and 13°, respectively.

Fig. 8(a) indicates that with θ_2 increasing from 10° to 30°, the axial displacement amplitudes of P_1, P_2, and P_3 reach their maximum values when θ_2 equals 24°. The axial displacement amplitudes of P_4, P_5, and P_6 decrease with the increase of θ_2. Furthermore, the circumferential displacement amplitudes of all the selected points increase slowly with the

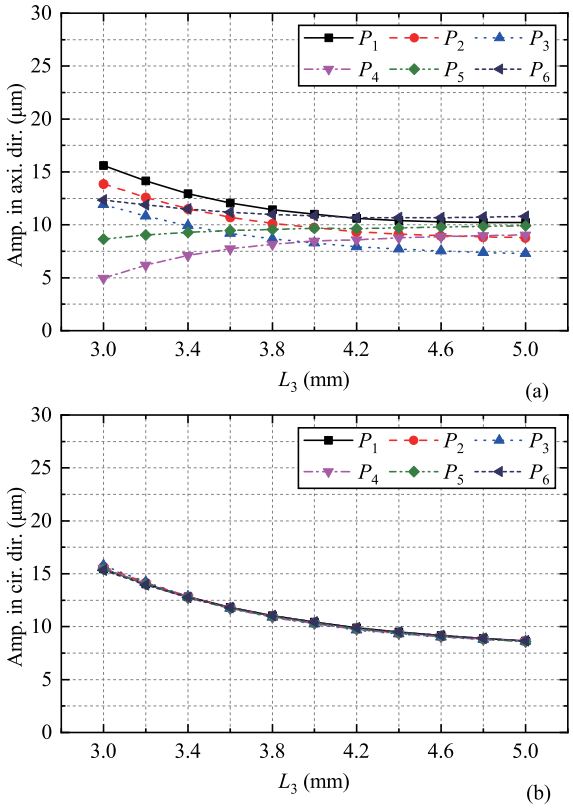

FIGURE 5. Displacement amplitudes of the selected points to different L_3. (a) Amplitudes in axial direction. (b) Amplitudes in circumferential direction.

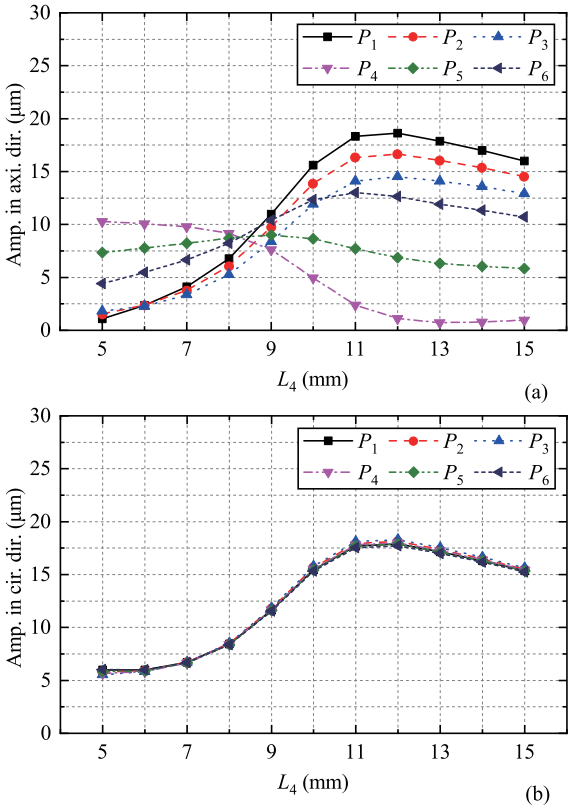

FIGURE 6. Displacement amplitudes of the selected points to different L_4. (a) Amplitudes in axial direction. (b) Amplitudes in circumferential direction.

increase of θ_2, and reach their maximum values when θ_2 is about 26°, as shown in Fig. 8(b).

It can be seen that increasing θ_3 leads to decreases in the circumferential displacement amplitudes of all the selected points and the axial displacement amplitudes of all the selected points except P_4, as shown in Fig. 9.

The results obtained by the modal analysis and harmonic analysis demonstrate that there are no significant differences between the circumferential displacement amplitudes of all the selected points for each parameter. However, the axial displacement amplitude of any point is quite different from that of any other point. Moreover, changes in the structural parameters of the proposed actuator have significant effects on the displacement amplitudes of the selected points in both directions. Based on the initial structure dimensions and the analysis results, the final structural dimensions are set as $L_1 = 40$ mm, $L_2 = 3$ mm, $L_3 = 3$ mm, $L_4 = 11$ mm, $\theta_1 = 20°$, $\theta_2 = 20°$, and $\theta_3 = 25°$. Under these dimensions, the mode shape of the actuator is shown in Fig. 10 and the resonance frequency was calculated to be 21.496 kHz.

IV. MOTIONS OF THE DRIVING TIPS

To verify the elliptical trajectories of the driving tips, transient analysis was adopted to plot the moving trajectories of the points P_1, P_2, P_3, P_4, P_5, and P_6. A sinusoidal signal with a frequency of 21.496 kHz and an amplitude of 150 V was applied to the PZT ceramic rings, and the end time for transient analysis was 5.4 ms. Fig. 11 shows the movement trajectories of the selected points obtained by the transient analysis. It can be seen that the elliptical trajectories of the selected points do not overlap well. The points P_4, P_5, and P_6 have larger maximum displacements in both directions than the points P_1, P_2, and P_3. In addition, compared to the points near the inner cylindrical surface of the actuator, P_3 and P_4, the points that near the outer cylindrical surface, P_1 and P_6, have bigger circumferential displacement amplitudes, which means that the points P_1 and P_6 have greater pushing effects on the rotor than the formers.

V. PROTOTYPE EXPERIMENTS

The prototype of the proposed piezoelectric actuator is shown in Fig. 12. As mentioned above, the points that near the outer cylindrical surface of the actuator have greater pushing effects on the rotor than the points near the inner cylindrical surface. To get better driving effect, the bottom surfaces of the rotors is designed to be circular ring type. Therefore, the contact parts between the rotor and the driving tips are located on the areas that near the outer cylindrical surface of the actuator. The rotary shaft is supported by two bearings and pushed by two rotors via flat keys. The preloads applied on the two rotors are provided by two preload springs of which compression amounts can be adjusted by two nuts.

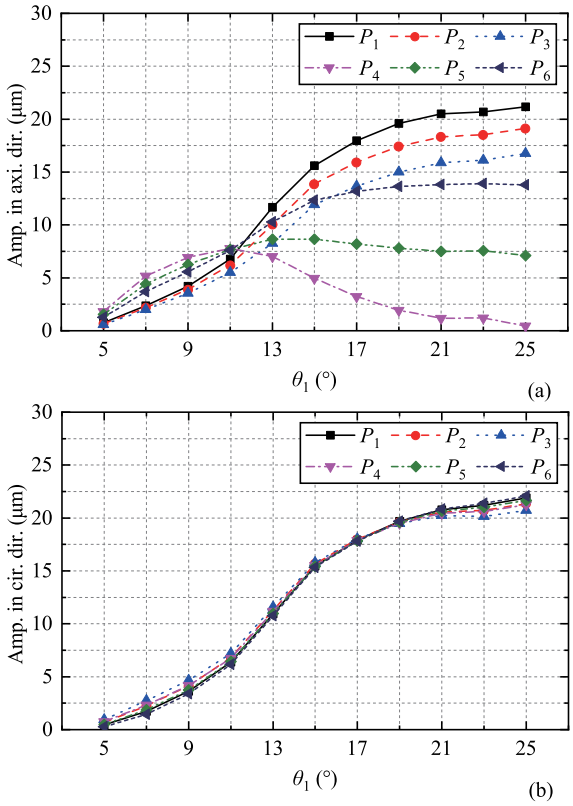

FIGURE 7. Displacement amplitudes of the selected points to different θ_1. (a) Amplitudes in axial direction. (b) Amplitudes in circumferential direction.

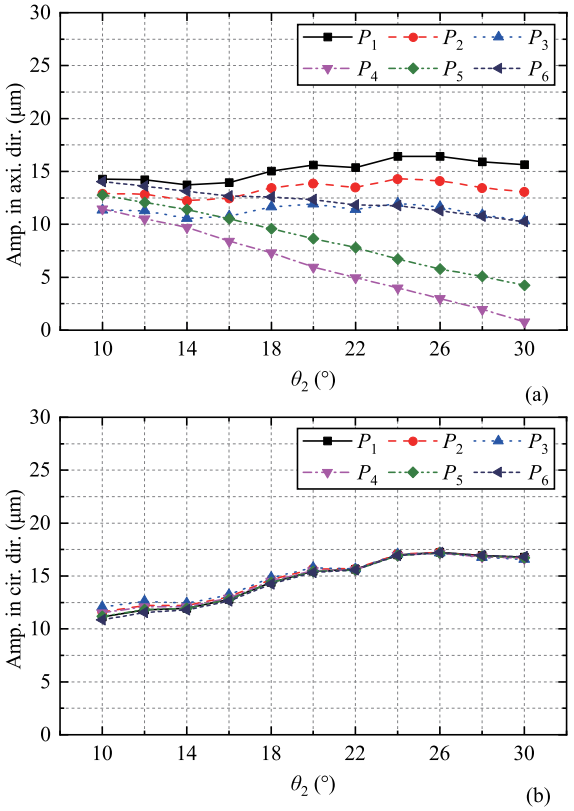

FIGURE 8. Displacement amplitudes of the selected points to different θ_2. (a) Amplitudes in axial direction. (b) Amplitudes in circumferential direction.

Several experiments were carried out to evaluate the output performance of the proposed actuator. Fig. 13 shows the impedance of the actuator versus frequency obtained by an impedance analyzer (E4990A, KEYSIGHT). The frequency corresponding to the minimum impedance was regarded as the resonance frequency of the actuator. The test result indicates that the resonance frequency is 21.135 kHz which is different from the result obtained by the modal analysis with a discrepancy of 0.361 kHz. The discrepancy is mainly caused by the differences between the real materials and the ideal model, the neglect of the electrodes in the modal analysis, and assembling errors.

A series of sinusoidal signals with the same voltage of 300 V_{P-P} and different frequencies were used to excite the actuator without the preload, respectively. Meantime, the vibration displacements of P_1 and P_6 under each excitation frequency were measured by a laser displacement sensor (LK-H020, KEYENCE) to get the optimum excitation frequency for the vibration displacements. Fig. 14 gives the curves of the displacement amplitudes of P_1 and P_6 in the axial and circumferential directions versus excitation frequency. It indicates that the amplitudes of P_1 and P_6 in both directions increase first and then decrease with the increase of the signal frequency, and reach their maximum values when the excitation frequency equals 20.765 kHz which was regarded as the optimum excitation frequency of the actuator for the vibration displacements. Fig. 15 gives the curves of the displacements of P_1 and P_6 in both directions under exciting of the optimum excitation frequency. The maximum displacements of P_1 in the axial and circumferential directions are 10 μm and 23.5 μm, respectively, and those of P_6 are 13.5 μm and 20.5 μm.

To obtain the optimum excitation frequency of the proposed actuator during pushing the rotors, no-load output speeds under different excitation frequencies were measured. Voltages of the excitation signals were set as 300 V_{P-P} and the preloads applied on the two rotors were both 7 N. The experimental results presented in Fig. 16 indicate that the no-load output speed increases first and then decreases with the increase of the signal frequency. The no-load output speed reaches to the maximum of 342 r/min, when the excitation frequency is 20.86 kHz. The optimum excitation frequency of the actuator during pushing the rotors is different from that for the vibration displacements with a discrepancy of 95 Hz which is mainly caused by the preloads applied on the rotors.

Fig. 17 shows the no-load out speeds of the rotors versus the voltage of the excitation signal applied on the PZT elements. An encoder which was linked to the rotary shaft was utilized to test the speed of the rotors. The preloads were set as 7 N, and the frequencies of the excitation signal were set as 20.86 kHz, 20.88 kHz, 20.90 kHz, 20.92 kHz, and 20.94 kHz,

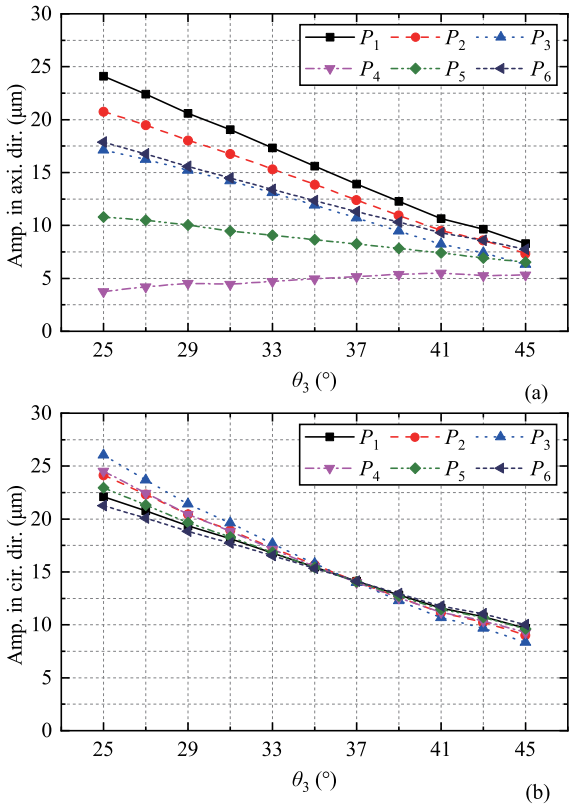

FIGURE 9. Displacement amplitudes of the selected points to different θ_3. (a) Amplitudes in axial direction. (b) Amplitudes in circumferential direction.

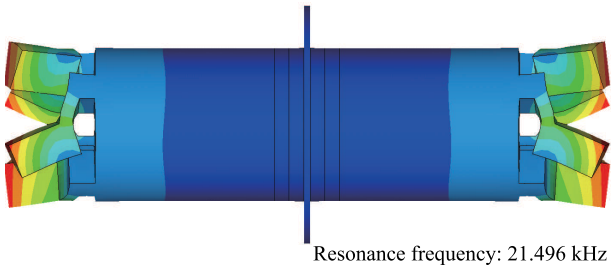

FIGURE 10. Mode shape of the actuator.

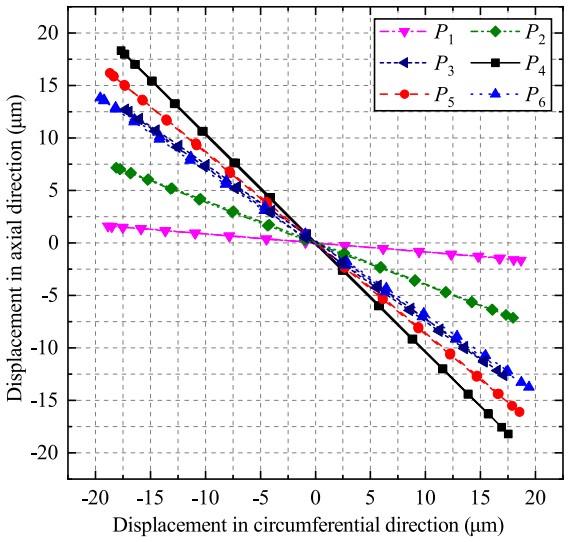

FIGURE 11. Movement trajectories of the selected points.

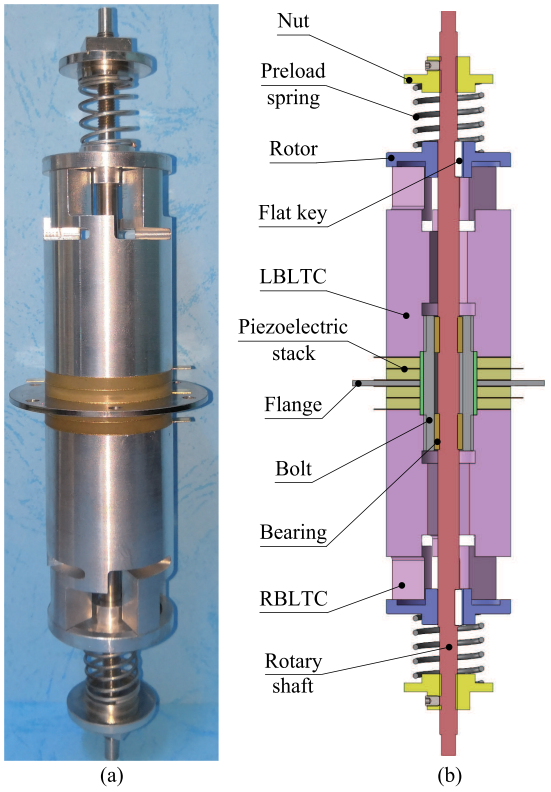

FIGURE 12. Prototype of the proposed piezoelectric actuator. (a) Photo of the piezoelectric actuator. (b) Sectional view of the piezoelectric actuator.

separately. We can see that the output speeds for all excitation frequencies increase with increasing voltage. A maximum value of 366 r/min is obtained when the frequency and voltage of the excitation signal are 20.86 kHz and 350 V_{P-P}, respectively.

Based on the assumption that the driving effect of dual-rotor drive is better than that of single-rotor drive, the prototype utilizes two rotors to drive the rotary shaft for rotary motions, as shown in Fig. 12. To verify this assumption, rotary speed versus load torque for the dual-rotor drive and single-rotor drive under different preloads were measured. Fig. 18 shows the schematic diagram of the experimental setup. An encoder was linked to the rotary shaft and utilized to measure the rotary speed. A string was wound to a loading wheel which was fixed on the rotary shaft. Therefore, via tying different weights with the string, different load torques, which were computed by multiplying the weights and the radius of the loading wheel together, were applied to the prototype. The voltage and frequency of the excitation signal were set as 350 V_{P-P} and 20.86 kHz, respectively. The preloads were set as 7 N and 11 N, separately, by adjusting the

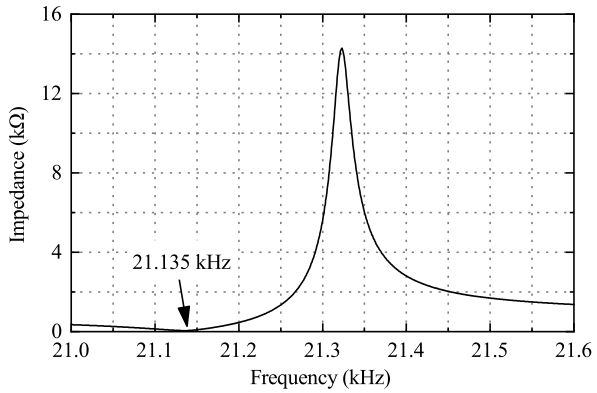

FIGURE 13. Impedance test results of the actuator.

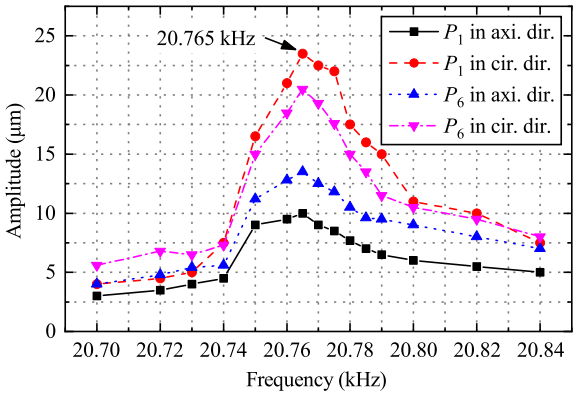

FIGURE 14. Displacement amplitudes of P_1 and P_6 in the axial and circumferential directions versus excitation frequency.

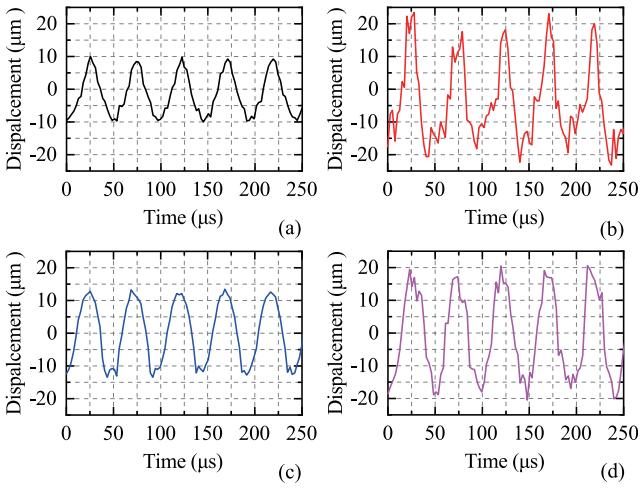

FIGURE 15. Displacements of P_1 and P_6 in both directions under exciting of the optimum excitation frequency. (a) P_1 in the axial direction. (b) P_1 in the circumferential direction. (c) P_6 in the axial direction. (d) P_6 in the circumferential direction.

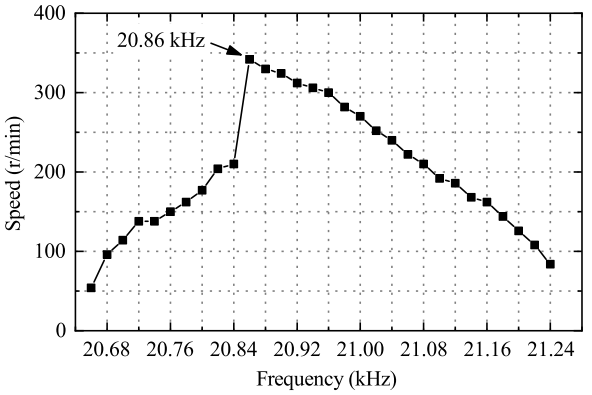

FIGURE 16. No-load output speed versus excitation frequency.

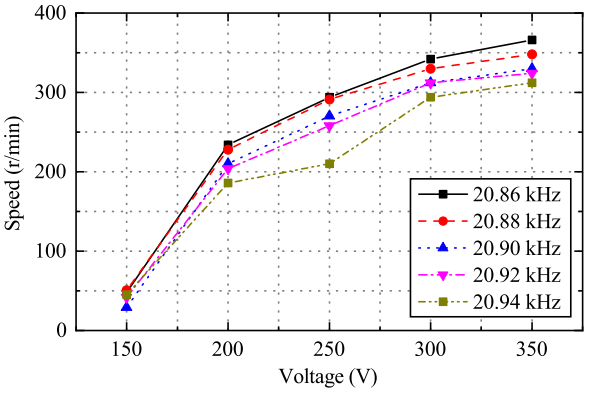

FIGURE 17. No-load output speed versus the voltage of the excitation signal.

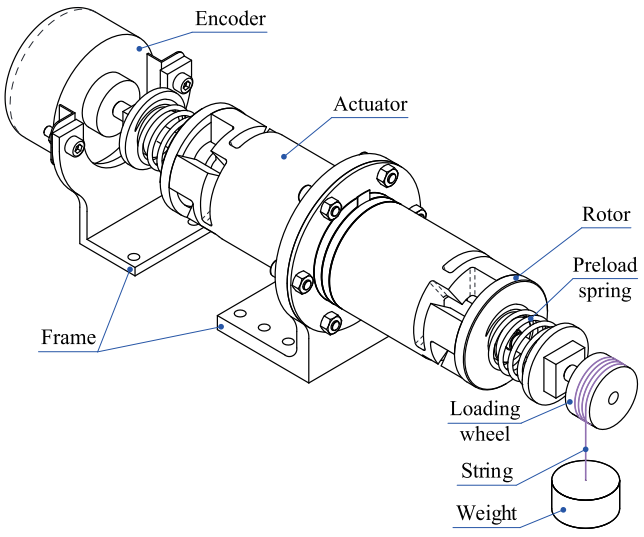

FIGURE 18. Schematic diagram of the experimental setup.

compression amount of the preload spring. Fig. 19 shows the curves of the speed versus output torque under the preloads of 7 N and 11 N for the dual-rotor drive and single-rotor drive. Experimental results show that all the rotary speeds for the two drive modes under different preloads decrease with increasing output torque. Furthermore, compared with the single-rotor drive, the dual-rotor drive reaches larger output torque under the preloads of 7 N or 11 N, which proves that the assumption is reasonable. When the preload is 11 N,

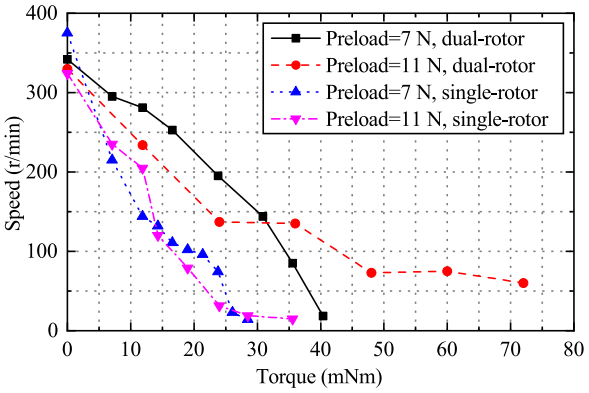

FIGURE 19. Plot of the rotary speed versus torque.

the maximum torque of 72 mN·m for the dual-rotor drive is achieved at the speed of 60 r/min.

VI. CONCLUSION

In this study, a bolt-clamped type piezoelectric actuator, which utilizes the hybrid of longitudinal and torsional vibrations to output rotary motions, was proposed and tested. This new rotary piezoelectric actuator uses two longitudinal-torsional convertors to transform part of the longitudinal vibrations, which is generated by one piezoelectric stack, into the torsional vibrations and generates elliptical motions at the ends of the driving tips. The structure dimensions of the two convertors, which have great influences on the effect of mode conversion, were determined by modal analysis and harmonic analysis. The transient analysis stated that the hybrid of longitudinal and torsional vibrations formed uniform elliptical motions on the driving tips. Several experiments were carried out to verify the vibration and output characteristics of the prototype. The optimum excitation frequency of the actuator for pushing the rotors was 20.86 kHz. The prototype obtained a peak no-load speed of 342 r/min with a preload of 11 N. Furthermore, the maximum torque of 72 mN·m was achieved at the speed of 60 r/min. Experimental results indicates that this new actuator is qualified to be used in the rotary drive. Besides, the application of one piezoelectric stack makes this new rotary actuator easy to excite. In future work, we will focus on the improvement of efficiency and application of this piezoelectric actuator.

REFERENCES

[1] W. Chen, X. Tian, K. Xue, S. Chen, and H. Yu, "An easily fabricated linear piezoelectric actuator using sandwich longitudinal vibrators with four driving feet," *IEEE Access*, vol. 7, pp. 4506–4515, 2018. doi: 10.1109/ACCESS.2018.2889807.

[2] J.-W. Wu, K.-C. Huang, M.-L. Chiang, M.-Y. Chen, and L.-C. Fu, "Modeling and controller design of a precision hybrid scanner for application in large measurement-range atomic force microscopy," *IEEE Trans. Ind. Electron.*, vol. 61, no. 7, pp. 3704–3712, Jul. 2014.

[3] H. Tang and Y. Li, "Development and active disturbance rejection control of a compliant micro-/nanopositioning piezostage with dual mode," *IEEE Trans. Ind. Electron.*, vol. 61, no. 3, pp. 1475–1492, Mar. 2014.

[4] W. Chen, Y. Liu, Y. Liu, X. Tian, X. Shan, and L. Wang, "Design and experimental evaluation of a novel stepping linear piezoelectric actuator," *Sens. Actuators A, Phys.*, vol. 276, pp. 259–266, Jun. 2018.

[5] Q. Zhang, W. Chen, Y. Liu, J. Liu, and Q. Jiang, "A frog-shaped linear piezoelectric actuator using first-order longitudinal vibration mode," *IEEE Trans. Ind. Electron.*, vol. 64, no. 3, pp. 2188–2195, Mar. 2017.

[6] A. Iula, L. Parenti, F. Fabrizi, and M. Pappalardo, "A high displacement ultrasonic actuator based on a flexural mechanical amplifier," *Sens. Actuators A, Phys.*, vol. 125, no. 2, pp. 118–123, Jan. 2006.

[7] D. Xu, Y. Liu, J. Liu, and W. Chen, "A bonded type ultrasonic motor using the bending of a crossbeam," *IEEE Access*, vol. 4, pp. 1109–1116, Mar. 2016.

[8] T. Morita, M. K. Kurosawa, and T. Higuch, "A cylindrical micro-ultrasonic motor," *Ultrasonics*, vol. 38, pp. 33–36, Mar. 2000.

[9] Z. Shen, Y. Liu, J. Zhao, X. Tang, and W. Chen, "Design and experiment of a small legged robot operated by the resonant vibrations of cantilever beams," *IEEE Access*, vol. 5, pp. 8451–8458, May 2017.

[10] H. Jalili, H. Salarieh, and G. Vossoughi, "Study of a piezo-electric actuated vibratory micro-robot in stick-slip mode and investigating the design parameters," *Nonlinear Dyn.*, vol. 89, no. 3, pp. 1927–1948, Aug. 2017.

[11] A. K. Eigoli and G. R. Vossoughi, "Locomotion modes of a novel piezo-driven microrobot: Analytical modeling and performance evaluation," *Mech. Mach. Theory*, vol. 52, pp. 248–266, Jun. 2012.

[12] G. Wang and Q. Xu, "Design and precision position/force control of a piezo-driven microinjection system," *IEEE/ASME Trans. Mechatronics*, vol. 22, no. 4, pp. 1744–1754, Aug. 2017.

[13] Y. L. Yang, Y.-D. Wei, J.-Q. Lou, F.-R. Xie, and L. Fu, "Development and precision position/force control of a new flexure-based microgripper," *J. Micromech. Microeng.*, vol. 26, no. 1, 2016, Art. no. 015005.

[14] M. N. M. Zubir and B. Shirinzadeh, "Development of a high precision flexure-based microgripper," *Precis. Eng.*, vol. 33, pp. 362–370, Oct. 2008.

[15] J. Li *et al.*, "Development of a novel parasitic-type piezoelectric actuator," *IEEE/ASME Trans. Mechatronics*, vol. 22, no. 1, pp. 541–550, Feb. 2017.

[16] C.-X. Li, Y. Ding, G.-Y. Gu, and L.-M. Zhu, "Damping control of piezo-actuated nanopositioning stages with recursive delayed position feedback," *IEEE/ASME Trans. Mechatronics*, vol. 22, no. 2, pp. 855–864, Apr. 2017.

[17] M. J. Yang, G.-Y. Gu, and L.-M. Zhu, "High-bandwidth tracking control of piezo-actuated nanopositioning stages using closed-loop input shaper," *Mechatronics*, vol. 24, no. 6, pp. 724–733, Sep. 2014.

[18] G. Y. Gu, L. M. Zhu, C. Y. Su, H. Ding, and S. Fatikow, "Proxy-based sliding-mode tracking control of piezoelectric-actuated nanopositioning stages," *IEEE/ASME Trans. Mechatronics*, vol. 20, no. 4, pp. 1956–1965, Aug. 2015.

[19] X. Wang, V. Pommier-Budinger, A. Reysset, and Y. Gourinat, "Simultaneous compensation of hysteresis and creep in a single piezoelectric actuator by open-loop control for quasi-static space active optics applications," *Control Eng. Pract.*, vol. 33, pp. 48–62, Dec. 2014.

[20] Y. Zhu, W. Liu, K. Jia, W. Liao, and H. Xie, "A piezoelectric unimorph actuator based tip-tilt-piston micromirror with high fill factor and small tilt and lateral shift," *Sens. Actuators A, Phys.*, vol. 167, no. 2, pp. 495–501, 2011.

[21] K. H. Koh, T. Kobayashi, F.-L. Hsiao, and C. Lee, "Characterization of piezoelectric PZT beam actuators for driving 2D scanning micromirrors," *Sens. Actuators A, Phys.*, vol. 162, no. 2, pp. 336–347, 2010.

[22] H. K. Ma, R. H. Chen, and Y. H. Hsu, "Development of a piezoelectric-driven miniature pump for biomedical applications," *Sens. Actuators A, Phys.*, vol. 234, pp. 23–33, Oct. 2015.

[23] M. Y. Zhou, Y. Ruan, W. T. Liu, S. Huang, and X. Fu, "A bio-inspired piezoelectric motor with simple structured asymmetric stator," *Smart Mater. Struct.*, vol. 23, no. 4, pp. 045003-1–045003-9, Feb. 2014.

[24] Q. Zhou, K. H. Lam, H. Zheng, W. Qiu, and K. K. Shung, "Piezoelectric single crystal ultrasonic transducers for biomedical applications," *Prog. Mater. Sci.*, vol. 66, pp. 87–111, Jun. 2014.

[25] D. De Lorenzo *et al.*, "Force feedback in a piezoelectric linear actuator for neurosurgery," *Int. J. Med. Robot. Comput. Assist. Surg.*, vol. 7, no. 3, pp. 268–275, 2011.

[26] H. Kunikata, Y. Tanaka, N. Aizawa, A. Nakagawa, T. Tominaga, and T. Nakazawa, "Experimental application of piezoelectric actuator-driven pulsed water jets in retinal vascular surgery," *Transl. Vis. Sci. Technol.*, vol. 3, no. 6, p. 10, 2014.

[27] S. Park and S. He, "Standing wave brass-PZT square tubular ultrasonic motor," *Ultrasonics*, vol. 52, no. 7, pp. 880–889, 2012.

[28] J. Z. Shi and B. Liu, "Optimum efficiency control of traveling-wave ultrasonic motor system," *IEEE Trans. Ind. Electron.*, vol. 58, no. 10, pp. 4822–4829, Oct. 2011.
[29] L. Wang, Q. Quan, K. Xue, and H. Li, "Development of a three-DOF piezoelectric actuator using a thin cross-beam vibrator," *Int. J. Mech. Sci.*, vol. 149, pp. 54–61, Dec. 2018.
[30] Q. Xu, "Robust impedance control of a compliant microgripper for high-speed position/force regulation," *IEEE Trans. Ind. Electron.*, vol. 62, no. 2, pp. 1201–1209, Feb. 2015.
[31] J. Deng, Y. Liu, J. Liu, D. Xu, and Y. Wang, "Development of a planar piezoelectric actuator using bending-bending hybrid transducers," *IEEE Trans. Ind. Electron.*, to be published. doi: 10.1109/TIE.2018.2873123.
[32] D. Huang, J.-X. Xu, V. Venkataramanan, and T. C. T. Huynh, "High-performance tracking of piezoelectric positioning stage using current-cycle iterative learning control with gain scheduling," *IEEE Trans. Ind. Electron.*, vol. 61, no. 2, pp. 1085–1098, Feb. 2014.
[33] Y. Liu, X. Yang, W. Chen, and D. Xu, "A bonded-type piezoelectric actuator using the first and second bending vibration modes," *IEEE Trans. Ind. Electron.*, vol. 63, no. 3, pp. 1676–1683, Mar. 2016.
[34] H. Tang *et al.*, "Development and repetitive-compensated PID control of a nanopositioning stage with large-stroke and decoupling property," *IEEE Trans. Ind. Electron.*, vol. 65, no. 5, pp. 3995–4005, May 2018.
[35] C. S. Zhao, *Ultrasonic Motors Technologies and Applications*. Beijing, China: Science Press, 2010, pp. 114–115.
[36] Y. X. Liu, J. P. Yan, L. Wang, and W. S. Chen, "A two-DOF ultrasonic motor using a longitudinal-bending hybrid sandwich transducer," *IEEE Trans. Ind. Electron.*, vol. 66, no. 4, pp. 3041–3050, Apr. 2019.
[37] M. Guo, S. Pan, J. Hu, C. Zhao, and S. Dong, "A small linear ultrasonic motor utilizing longitudinal and bending modes of a piezoelectric tube," *IEEE Trans. Ultrason., Ferroelect., Freq. Control*, vol. 61, no. 4, pp. 705–709, Apr. 2014.
[38] X. T. Tang, Y. X. Liu, S. J. Shi, W. S. Chen, and X. D. Qi, "Development of a novel ultrasonic drill using longitudinal-bending hybrid mode," *IEEE Access*, vol. 5, pp. 7362–7370, Jun. 2017.
[39] J. J. Wang, J. F. Zhang, P. F. Feng, P. Guo, and Q. L. Zhang, "Feasibility study of longitudinal-torsional-coupled rotary ultrasonic machining of brittle material," *J. Manuf. Sci. Eng*, vol. 140, no. 5, pp. 051008-1–051008-11, Mar. 2018.
[40] L. Yang and C. S. Zhao, "Flexible supporting and fixing method for hybrid ultrasonic motor using longitudinal and torsional vibration modes," *J. Vibroeng.*, vol. 16, no. 6, pp. 2854–2861, Sep. 2014.
[41] X. Li, P. Ci, G. Liu, and S. Dong, "A two-layer linear piezoelectric micromotor," *IEEE Trans. Ultrason., Ferroelectr., Freq. Control*, vol. 62, no. 3, pp. 405–411, Mar. 2015.
[42] K. Nakamura, M. Kurosawa, and S. Ueha, "Characteristics of a hybrid transducer-type ultrasonic motor," *IEEE Trans. Ultrason., Ferroelectr., Freq. Control*, vol. 38, no. 3, pp. 188–193, May 1991.
[43] Y. Tomikawa, K. Adachi, M. Aoyagi, T. Sagae, and T. Takano, "Some constructions and characteristics of rod-type piezoelectric ultrasonic motors using longitudinal and torsional vibrations," *IEEE Trans. Ultrason., Ferroelectr., Freq. Control*, vol. 39, no. 5, pp. 600–608, Sep. 1992.
[44] J. Tsujino and A. Suzuki, "Load characteristics of ultrasonic motor with a longitudinal-torsional converter and various nonlinear springs for inducing static pressure," in *Proc. IEEE Ultrason. Symp.*, pp. 545–550, Oct. 2001.
[45] P. Harkness, M. Lucas, and A. Cardon, "Coupling and degenerating modes in longitudinal-torsional step horns," *Ultrasonics*, vol. 52, no. 8, pp. 980–988, Dec. 2012.
[46] L. Wang, J. K. Liu, Y. X. Liu, X. Q. Tian, and J. P. Yan, "A novel single-mode linear piezoelectric ultrasonic motor based on asymmetric structure," *Ultrasonics*, vol. 89, pp. 137–142, Sep. 2018.
[47] X. H. Yang, Y. X. Liu, W. S. Chen, and J. K. Liu, "Sandwich-type multi-degree-of-freedom ultrasonic motor with hybrid excitation," *IEEE Access*, vol. 4, pp. 905–913, Mar. 2016.
[48] T. Nishimura, H. Hosaka, and T. Morita, "Resonant-type smooth impact drive mechanism (SIDM) actuator using a bolt-clamped Langevin transducer," *Ultrasonics*, vol. 52, no. 1, pp. 75–80, Jan. 2012.
[49] Y. Liu, W. Chen, X. Yang, and J. Liu, "A rotary piezoelectric actuator using the third and fourth bending vibration modes," *IEEE Trans. Ind. Electron.*, vol. 61, no. 8, pp. 4366–4373, Aug. 2014.

DEEN BAI was born in Shandong, China, in 1987. He received the B.S. degree from Northeast Forestry University, Harbin, China, in 2011, and the M.S. degree in mechanical engineering from the Harbin Institute of Technology, Harbin, China, in 2014, where he is currently pursuing the Ph.D. degree in mechanical engineering. His research interests include rotary-percussive ultrasonic drills and crushing efficiency for rock.

QIQUAN QUAN was born in Anhui, China, in 1983. He received the B.S. and M.S. degrees from the Harbin Institute of Technology, Harbin, China, in 2005 and 2007, respectively, and the Ph.D. degree from Ritsumeikan University, Japan. He is currently an Associate Professor with the State Key Laboratory of Robotics and System, Harbin Institute of Technology. His current research interest includes in-orbit and on-ground testing of the aerospace mechanism.

DEWEI TANG was born in Heilongjiang, China, in 1966. He received the master's degree and the Ph.D. degree in mechanical engineering from the Harbin Institute of Technology, Harbin, China, in 1991 and 2000, respectively, where he is currently a Professor with the State Key Laboratory of Robotics and System. His current research interests include drilling performance analyses and enhancement in extreme environments and undisturbed sampling technique.

ZONGQUAN DENG was born in 1956. He received the B.S. and M.S. degrees from the Harbin Institute of Technology, Harbin, China, in 1982 and 1984, respectively, where he is currently a Professor with the State Key Laboratory of Robotics and System. His current research interests include special robot systems and aerospace mechanisms and control.